Oceanic Detachment Faults Generate Compression in Extension

R. Parnell-Turner[1], R. A. Sohn[1], C. Peirce[2], T. J. Reston[3], C. J. MacLeod[4], R. C. Searle[2] and N. M. Simão[2].

[1] Department of Geology & Geophysics, Woods Hole Oceanographic Institution, Woods Hole Road, Woods Hole, MA 02543, USA

[2] Department of Earth Sciences, Durham University, South Road, Durham, DH1 3LE, UK

[3] School of Geography, Earth and Environmental Sciences, University of Birmingham, Birmingham B15 2TT, UK

[3] School of Earth & Ocean Sciences, Cardiff University, Main Building, Park Place, Cardiff, CF10 3AT, UK

ABSTRACT

In extensional geologic systems such as mid-ocean ridges, deformation is typically accommodated by slip on normal faults, where material is pulled apart under tension and stress is released by rupture during earthquakes and magmatic accretion. However, at slowly spreading mid-ocean ridges where the tectonic plates move apart at rates less than 80 km Ma^{-1}, these normal faults may roll over to form long-lived, low-angled detachments that exhume mantle rocks and form corrugated domes on the seabed. Here we present the results of a local microearthquake study over an active detachment at 13°20'N on the Mid-Atlantic Ridge to show that these features can give rise to reverse faulting earthquakes in response to plate bending. During a six-month survey period we observed a remarkably high rate of seismic activity, with more than 244,000 events detected along 25 km of the ridge axis, to depths of ~10 km below seafloor. Surprisingly, the majority of these were reverse faulting events. Restricted to depths of 3 - 6 km below seafloor, these reverse events delineate a band of intense compressional seismicity located adjacent to a zone of deeper extensional events. This deformation pattern is consistent with flexural models of plate bending during lithospheric accretion. Our results

indicate that the lower portion of the detachment footwall experiences compressive stresses and deforms internally as the fault rolls over to low angles before emerging at the seafloor. These compressive stresses trigger reverse faulting even though the detachment itself is an extensional system.

INTRODUCTION

Oceanic lithosphere is formed at mid-ocean ridges by a combination of magmatism and normal faulting, driven by far-field forces arising from processes including plate subduction and mantle convection (Lachenbruch, 1976). In these extensional settings, a portion of the strain is expected to be accommodated by slip on normal faults, which is reflected in the focal mechanisms of earthquakes observed near the spreading axis (Sykes, 1967). At slow-spreading ridges, accounting for large parts of the lithosphere formed in the Atlantic, Indian and Arctic Oceans, young lithosphere may be deformed by slip along large-offset normal faults called detachments (Cann et al., 1997; Tucholke et al., 1998; Dick et al., 2003; Escartin et al., 2008b). Detachment faults can exhume lower crustal gabbros and serpentinized mantle peridotites at the seabed and form kilometer-scale dome-shaped features called oceanic core complexes (Cann et al., 1997; MacLeod et al., 2002; Escartin et al., 2003; Grimes et al., 2008). The mechanical behavior of detachment faults is controversial because the domed fault surfaces emerge from the seafloor at low angles that are that are incompatible with the physics of extensional faulting (Buck et al., 2005). There is evidence for fault initiation on a steeply dipping, deeply penetrating rupture surface (MacLeod et al., 2009; Morris et al., 2009; MacLeod et al., 2011), but the mechanism by which the fault rolls over to low angles prior to seafloor exhumation is poorly understood. Local earthquake surveys with ocean bottom seismographs (OBSs) have the potential to address this issue; however, previous OBS deployments at oceanic detachments had insufficient aperture and instrument density to resolve the mechanics of fault rollover (deMartin et al., 2007; Collins et al., 2012; Grevemeyer et al., 2013). Intriguingly, a few reverse faulting events were observed beneath the Logatchev core complex on the Mid-Atlantic Ridge (MAR) at 14°40'N, but the relationship of these events to the extensional fault system was unclear, and they were attributed to volume

expansion from serpentinization or magma chamber filling rather than deformation on a detachment fault (Grevemeyer et al., 2013).

MICROEARTHQUAKE EXPERIMENT

In 2014 we conducted the largest microearthquake experiment to-date at a slow-spreading ridge. A dense network of 25 short-period OBSs (instrument spacing of 2-3 km) was deployed for a six-month period along ~10 km of the ridge axis at 13°N on the MAR (Fig. 1). Detachment faults are common in this region, including two well-surveyed and sampled oceanic core complexes located at 13°20'N and 13°30'N (Smith et al., 2006; MacLeod et al., 2009; Mallows and Searle, 2012; Escartin et al., 2017). Both core complexes have well-developed, domed, corrugated surfaces and are accompanied by a high level of hydroacoustically-recorded seismicity, suggesting that they are currently active or have been in the recent geological past (Smith et al., 2008; MacLeod et al., 2009; Mallows and Searle, 2012).

We recorded over 244,000 events on more than three stations during the 198 day deployment, yielding a mean rate of ~1240 microearthquakes per day (see Methods), two orders of magnitude greater than that observed at the Logatchev core complex (Grevemeyer et al., 2013). This remarkably high rate of seismicity was fairly constant throughout the deployment period (Fig. 2b). There was no evidence for foreshock-main shock sequences, except for a small seismic swarm in the western band of events at Julian day 280 within a region extending 3 km south from its northern tip. The locations and focal mechanisms of these events are indistinguishable from the rest of the seismicity in this area. Events have small local magnitude (M_L), ranging between -1.0 and 2.7 and with a modal average of 0.3 (Supplementary Fig. 1). The high number of earthquakes, combined with the dense seismic network, allowed us to estimate hypocenters and focal mechanism solutions for a subset of 35,262 well-characterized events (see Appendix). These reveal that reverse faulting was the most common mode of deformation near the 13°20’N detachment during our deployment (Fig. 1). The compressional events define a distinct arc of intense seismicity that wraps around the detachment trace (on the eastern edge of the corrugated surface), at depths of 3-6 km beneath the seabed (Fig. 2 and

Supplementary Fig. 2). The slip directions (i.e., rake) of these events are typical of reverse and reverse-oblique faults. The compression (*P*) axes are dominantly sub-horizontal but there is no preferred orientation for the dip and strike of the fault planes (Fig. 2c). Events within the reverse faulting band of seismicity have slightly smaller magnitudes than those in the normal faulting band (Supplementary Fig. 1). In contrast, normal faulting is restricted to a narrow band of seismicity ~3 km east of the reverse faulting zone, at depths of 5-12 km beneath the seabed (Fig. 2 and Supplementary Fig. 2). These event depths, which are comparable to the depth of normal faulting seismicity observed at the TAG detachment (deMartin et al., 2007), clearly show that extensional faulting extends beneath the crust. Focal mechanisms indicate steeply-dipping (50-70°) normal faults oriented sub-parallel to the near N-S trending spreading axis (Mallows and Searle, 2012) (Fig. 2c), and tension (*T*) axes indicating consistent extensional stress oriented parallel to the spreading direction (~273°).

DISCUSSION

Our observations indicate that lithospheric extension at the 13°20'N detachment generates both compressional and extensional seismicity contemporaneously. The band of intense reverse faulting at 3-6 km depth is located directly beneath the hanging wall cutoff, where the gently-dipping corrugated surface emerges on the seafloor (Fig. 2e), hence cannot lie on the detachment fault plane itself. Instead, this reverse faulting must be occurring within the detachment footwall. An active high-temperature vent field is located on the 1320 corrugated surface (Escartin et al., 2017), which could indicate footwall emplacement of magma bodies (Fig. 1); however, the vent site is located 2.3 km west from the band of reverse faulting (Fig. 2e), and cooling of a magma body should generate tensile, rather than compressive, stresses. Thermal contraction associated with heat extraction from a footwall magma body is therefore not a plausible source mechanism for the shallow band of compressive seismicity. Our observations instead support a model in which internal deformation of the lithosphere in response to flexural bending stress results in a high level of seismicity at the point of maximum bending (Lavier et al., 1999; Buck et al., 2005). The variability in the strike and dip of fault plane

solutions (*P*- and *T*-axes) in this zone indicates distributed, isotropic deformation of the deeper, internal portion of the detachment footwall (Fig. 2c). In contrast, towards the center of the axial valley and at greater depth (6-10 km), steep, ridge-parallel normal faulting accommodates extensional deformation on the active detachment as new material accretes into the footwall. The short distance between bands of reverse and normal faulting (~2 km perpendicular to the fault plane) requires a rapid change in the footwall stress field, from extensional stresses in the accretion zone to compressive stresses in the region of fault rollover. This observation, combined with the spatially restricted zone of reverse faulting, indicates that fault rollover may be a relatively abrupt, rather than gradual, process, with tightening of curvature at progressively shallower sub-surface depths.

We have developed a simple model based upon the deflection of a bending plate with elastic-plastic rheology to reconcile our observations (see Supplementary Materials; McAdoo et al., 1978). The model is constrained by the location and dip of the corrugated fault surface at the seafloor, the spatial distribution and focal mechanisms of observed earthquakes, and a lithospheric slab thickness of 6 km inferred from the depth distribution of seismicity. We use the distribution of earthquakes in the footwall to define a stress profile, with 'plastic' failure at depths where seismic events are observed (in elastic-plastic models, deformation from earthquakes is treated as bulk 'plastic' yielding), and assume that the initiating fault is likely to have a maximum dip of ~70°. We seek a bending profile that satisfies these constraints, by varying the mechanical strength of the plate in terms of its flexural rigidity, or effective elastic thickness (T_e). We find that a best fit is obtained if T_e increases linearly from 0.7 km near the spreading axis, to 0.9 km at the point where the footwall emerges at the seafloor (dashed line, Fig. 2e). This range in T_e, which is a modeling parameter rather than a physical property of the lithosphere, is consistent with previous estimates from bathymetric profiles of detachment faulted terrain (Schouten et al., 2010). Our simple model demonstrates that the location of the reverse faulting is consistent with that predicted by bending of the detachment footwall under a mechanically reasonable deflection profile (Fig. 3).

The two bands of seismicity show well-defined along-axis extents, the northern ends of which lie within the OBS network and are therefore well resolved. The extent of

the western, compressional band roughly matches that of the corrugated surface between 13°15’ and 13°21’N, north of which the NVZ begins to develop (Fig. 1). The band of normal faulting extends ~3 km further north to 13°23’N, beyond which the seismicity rate is remarkably low. These results demonstrate that the nature of seismically accommodated deformation changes significantly at the northern limit of the 1320 core complex, but the inability of our network to provide focal mechanism solutions in this area makes it difficult to interpret this change in the context of fault structure and deformation. A vigorous swarm of seismicity occurred over a 2-3 day period at 13°27’N, just south of the 1330 core complex, which is suggestive of magmatic activity; however, this interpretation is necessarily tentative because we cannot obtain focal mechanism estimates from this area.

The apparent lack of seismicity on the upper surface of the detachment footwall at shallow crustal depths is enigmatic. Extensional bending stresses are clearly high in this region, and there must be slip between the footwall and hanging wall on the fault surface. Rock samples recovered from the 13°20’N detachment fault scarp are dominated by hydrothermal quartz-cemented basalt breccia, in addition to sheared serpentinites, talc schists, incohesive cataclasites and hydrothermal deposits (MacLeod et al., 2009; Escartin et al., 2014, 2017). This assemblage provides evidence for significant hydrothermal alteration and mineralization in the fault zone, which may modify the rheology of these rocks and preclude the generation of detectable seismicity (Reinen et al., 1992; Escartin et al., 2008a). Alternatively, we cannot rule out the possibility that deformation in this zone occurs episodically over time intervals that are long compared to the duration of our observations.

CONCLUSIONS

We find that accretion and extension of oceanic crust at the 13°20'N detachment is accommodated by two distinct modes of deformation, reflecting two stages of lithospheric evolution. First, extensional faulting occurs at the point where the detachment fault initiates at depths of 6-10 km. These high-angle normal faults accommodate the far-field forces that drive plate separation as lower crustal and upper

mantle rocks are incorporated into newly forming lithosphere in the rising fault footwall. Second, as the footwall rotates to lower angles, bending stresses lead to internal compression in the lower half of the plate. As a result, reverse faults initiate within the bending lithosphere at depths of 3 to 6 km below where the footwall emerges at the seafloor to form a domed, corrugated fault surface (Fig. 3). This evolution of footwall stress is consistent with kinematic models for detachment fault behavior (Buck, 1988) and with direct observations for reverse faulting in detachment fault footwalls (Pressling et al., 2012), suggesting that reverse faulting may be ubiquitous in mature, active oceanic detachments. Our results provide a new framework for interpreting detachment seismicity, and suggest that reverse faulting events reported at other core complexes may have been triggered by bending stresses rather than volume expansion (e.g., serpentinization). The mechanical regime we describe shows that plate bending associated with the exhumation and formation of oceanic core complexes can generate compressional stresses leading to reverse faulting, despite being situated in an extensional stress regime.

REFERENCES CITED

Buck, W.R., 1988, Flexural Rotation of Normal Faults: Tectonics, v. 7, no. 5, p. 959–973, doi: 10.1029/TC007i005p00959.

Buck, W.R., Lavier, L., and Poliakov, A.N.B., 2005, Modes of faulting at mid-ocean ridges: Nature, v. 434, p. 719–723, doi: 10.1038/nature03358.

Cann, J.R., Blackman, D.K., Smith, D.K., McAllister, E., Janssen, B., Mello, S., Avgerinos, E., Pascoe, A.R., and Escartin, J., 1997, Corrugated slip surfaces formed at ridge-transform intersections on the Mid-Atlantic Ridge: Nature, v. 385, p. 329–332.

Collins, J.A., Smith, D.K., and Mcguire, J.J., 2012, Seismicity of the Atlantis Massif detachment fault, 30°N at the Mid-Atlantic Ridge: Geochem. Geophys. Geosyst., v. 13, no. 1, doi: 10.1029/2012GC004210.

deMartin B. J., Sohn, R.A., Canales, J.P., and Humphris, S.E., 2007, Kinematics and geometry of active detachment faulting beneath the Trans-Atlantic Geotraverse (TAG) hydrothermal field on the: Geology, v. 35, p. 711–714, doi: 10.1130/G23718A.1.

Dick, H.J.B., Lin, J., and Schouten, H., 2003, An ultraslow-spreading class of ocean ridge: Nature, v. 426, p. 405–412.

Escartin, J., Andreani, M., Hirth, G., and Evans, B., 2008a, Relationships between the microstructural evolution and the rheology of talc at elevated pressures and temperatures: Earth Planet. Sci. Lett., v. 268, no. 3–4, p. 463–475, doi: 10.1016/j.epsl.2008.02.004.

Escartin, J., Bonnemains, D., Mevel, C., Cannat, M., Petersen, S., Augustin, N., Bezos,

A., Chavagnac, V., Choi, Y., Godard, M., Haaga, K., Hamelin, C., Ildefonse, B., Jamieson, J., et al., 2014, Insights into the internal structure and formation of striated fault surfaces of oceanic detachments from in situ observations (13°20'N and 13°30'N, Mid-Atlantic Ridge): Abstract T54A-01 presented at 2014 Fall Meeting, AGU, San Francisco, Calif. 9-13 Dec,.

Escartin, J., Mével, C., MacLeod, C.J., and McCaig, A.M., 2003, Constraints on deformation conditions and the origin of oceanic detachments: The Mid-Atlantic Ridge core complex at 15°45′N: Geochem. Geophys. Geosyst., v. 4, no. 8, doi: 10.1029/2002GC000472.

Escartin, J., Petersen, S., Bonnemains, D., Cannat, M., Andreani, M., Bezos, A., Chavagnac, V., Choi, Y., Godard, M., Haaga, K., Hamelin, C., Ildefonse, B., Jamieson, J., John, B., et al., 2017, Tectonic structure, evolution, and the nature of oceanic core complexes and their detachment fault zones (13°20' N and 13°30'N, Mid Atlantic Ridge): Geochem. Geophys. Geosyst., v. 18, doi: 10.1002/2016GC006775.

Escartin, J., Smith, D.K., Cann, J.R., Schouten, H., Langmuir, C.H., and Escrig, S., 2008b, Central role of detachment faults in accretion of slow-spreading oceanic lithosphere: Nature, v. 455, no. 7214, p. 790–794, doi: 10.1038/nature07333.

Grevemeyer, I., Reston, T.J., and Moeller, S., 2013, Microseismicity of the Mid-Atlantic Ridge at 7°S – 8°15'S and at the Logatchev Massif oceanic core complex at 14°40'N-14°50'N: Geochem. Geophys. Geosyst., v. 14, no. 9, doi:10.1002/ggge.20197.

Grimes, C.B., John, B.E., Cheadle, M.J., and Wooden, J.L., 2008, Protracted construction

of gabbroic crust at a slow spreading ridge: Constraints from 206Pb/238U zircon ages from Atlantis Massif and IODP Hole U1309D (30°N, MAR): Geochem. Geophys. Geosyst., v. 9, no. 8, doi:10.1029/2008GC002063.

Lachenbruch, A.H., 1976, Dynamics of a Passive Spreading Center: J. Geophys. Res., v. 81, no. 11, p. 1883–1902.

Lavier, L., Buck, W.R., and Poliakov, A., 1999, Self-consistent rolling-hinge model for the evolution of large-onset low-angle normal faults: Geology, v. 27, no. 12, p. 1127–1130, doi: 10.1130/0091-7613

MacLeod, C.J., Carlut, J., Escartin, J., Horen, H., and Morris, A., 2011, Quantitative constraint on footwall rotations at the 15°45′N oceanic core complex, Mid-Atlantic Ridge: Implications for oceanic detachment fault processes: Geochem. Geophys. Geosyst., v. 12, no. 5, doi: 10.1029/2011GC003503.

MacLeod, C.J., Escartin, J., Banerji, D., Banks, G.J., Gleeson, M., Irving, D.H.B., Lilly, R.M., McCaig, A.M., Niu, Y., Allerton, S., and Smith, D.K., 2002, Direct geological evidence for oceanic detachment faulting: The Mid-Atlantic Ridge, 15 45′ N: Geology, v. 30, no. 10, p. 879–882, doi: 10.1130/0091-7613(2002)030<0879.

MacLeod, C.J., Searle, R.C., Murton, B.J., Casey, J.F., Mallows, C., Unsworth, S.C., Achenbach, K.L., and Harris, M., 2009, Life cycle of oceanic core complexes: Earth Planet. Sci. Lett., v. 287, no. 3–4, p. 333–344, doi: 10.1016/j.epsl.2009.08.016.

Mallows, C., and Searle, R.C., 2012, A geophysical study of oceanic core complexes and surrounding terrain, Mid-Atlantic Ridge 13°N-14°N: Geochem. Geophys. Geosyst., v. 13, doi: 10.1029/2012GC004075.

McAdoo, D.C., Caldwell, J.G., and Turcotte, D.L., 1978, On the elastic-perfectly plastic

bending of the lithosphere under generalized loading with application to the Kuril Trench: Geophys. J. Int., v. 54, no. 1, p. 11–26, doi: 10.1111/j.1365-246X.1978.tb06753.x.

Minshull, T.A., Sinha, M.C., and Peirce, C., 2005, Multi-disciplinary, sub-seabed geophysical imaging: Sea Technology, v. 46, no. 10, p. 27–31.

Morris, A., Gee, J.S., Pressling, N., John, B.E., MacLeod, C.J., Grimes, C.B., and Searle, R.C., 2009, Footwall rotation in an oceanic core complex quantified using reoriented Integrated Ocean Drilling Program core samples: Earth Planet. Sci. Lett., v. 287, no. 1–2, p. 217–228, doi: 10.1016/j.epsl.2009.08.007.

Pressling, N., Morris, A., John, B.E., and MacLeod, C.J., 2012, The internal structure of an oceanic core complex: An integrated analysis of oriented borehole imagery from IODP Hole U1309D (Atlantis Massif): Geochem. Geophys. Geosyst., v. 13, no. 4, doi: 10.1029/2012GC004061.

Reinen, A., Tullis, E., and Weeks, D., 1992, Two-mechanism model for frictional sliding of serpentinite: Geophys. Res. Lett., v. 19, no. 15, p. 1535–1538.

Schouten, H., Smith, D.K., Cann, J.R., and Escartin, J., 2010, Tectonic versus magmatic extension in the presence of core complexes at slow-spreading ridges from a visualization of faulted seafloor topography: Geology, v. 38, no. 7, p. 615–618, doi: 10.1130/G30803.1.

Simão, N., Peirce, C., Falder, M., Reston, T.J., Macleod, C.J., and Searle, R.C., 2016, Velocity structure of the crust at 13°N on the Mid-Atlantic Ridge: implications for crustal accretion and oceanic core complex formation: Abstract T33A-2997 presented at 2016 Fall Meeting, AGU, San Francisco, Calif. 12-16 Dec,.

Smith, D.K., Cann, J.R., and Escartin, J., 2006, Widespread active detachment faulting and core complex formation near 13°N on the Mid-Atlantic: Nature, v. 442, p. 440–443, doi: 10.1038/nature04950.

Smith, D.K., Escartin, J., Schouten, H., and Cann, J.R., 2008, Fault rotation and core complex formation: Significant processes in seafloor formation at slow-spreading mid-ocean ridges (Mid-Atlantic Ridge, 13°–15°N): Geochem. Geophys. Geosyst., v. 9, no. 3, doi: 10.1029/2007GC001699.

Sykes, L.R., 1967, Mechanism of earthquakes and nature of faulting on the mid-oceanic ridges: J. Geophys. Res., v. 72, no. 8, p. 2131–2153, doi: 10.1029/JZ072i008p02131.

Tucholke, B.E., Lin, J., and Kleinrock, M.C.C., 1998, Megamullions and mullion structure defining oceanic metamorphic core complexes on the Mid-Atlantic Ridge: J. Geophys. Res., v. 103, no. B5, p. 9857–9866.

ACKNOWLEDGEMENTS

This research was funded by NERC grants NE/J02029X/1, NE/J021741/1 and NE/J022551/1, and by NSF grant OCE-1458084. Instruments were provided by the NERC UK Ocean-Bottom Instrumentation Facility (Minshull et al., 2005). We are grateful to the officers, crew, technicians and science parties of RRS *James Cook* cruises JC102, JC109 and JC132 for their hard work and professionalism.

FIGURE CAPTIONS

Figure 1. Bathymetric map with seismicity and focal mechanisms at 13°20'N on the MAR. Inset shows location of study site (red box) and mid-ocean ridges (black lines). Main panel shows seismicity rate calculated in 100 x 100 m bins for 18,313 well constrained, relocated events detected by >9 instruments. Randomly selected first-motion focal mechanism solutions are plotted in lower-hemisphere projection; red line shows neovolcanic zone (NVZ); pink triangles show OBS positions; white triangle is Irinovskoe vent field. Location of along-axis adjacent corrugated oceanic core complexes shown by 1320 and 1330 labels, cross shows average 68% confidence level horizontal location uncertainty (0.9 km).

Figure 2. Seismicity rate and cross-sections. a: Shaded-relief bathymetry (illuminated from NE) with cumulative seismic moment release in dyn cm^{-1}; red/blue polygons delineate domains shown in b and c; black lines are transects shown in d and e; white triangle is vent field; red line is NVZ. b: Seismicity time series for domains 1 (blue) and 2 (red). c: Stereonets with P (black) and T (gray) axes for events in domains 1 and 2; gray shading is best-fitting fault plane solution for domain 2 (352° strike and 72° dip east). d and e: Cross-sections with hypocenters colored by domain as in (a) and representative focal mechanisms (cross-sections through lower hemisphere projection). Black solid line is seabed; thickened sections indicate corrugated fault scarp exposure; dashed line is calculated plate deflection from elastic-plastic model, applicable to spreading parallel profile in (e) only; arrows show location of hanging wall cutoff (HWC) and nearest along-strike projection of the neovolcanic zone (NVZ).

Figure 3. Schematic diagram of stress fields generated by deformation at mature oceanic detachment faults. Most of lithosphere is under tension, but bending (M) associated with fault rollover to low dip angles generates compressive stresses (red shading) in lower portion of fault footwall. Gray dotted lines are markers perpendicular to fault surface; gray dashed line shows nominal base of lithosphere. Earthquakes are expected in zones where stress exceeds yield stress ($|\sigma| > |\sigma 0|$), consistent with our observations. Hanging wall is tectonized and thus weak, which facilitates penetration of seawater into upper part of fault zone.

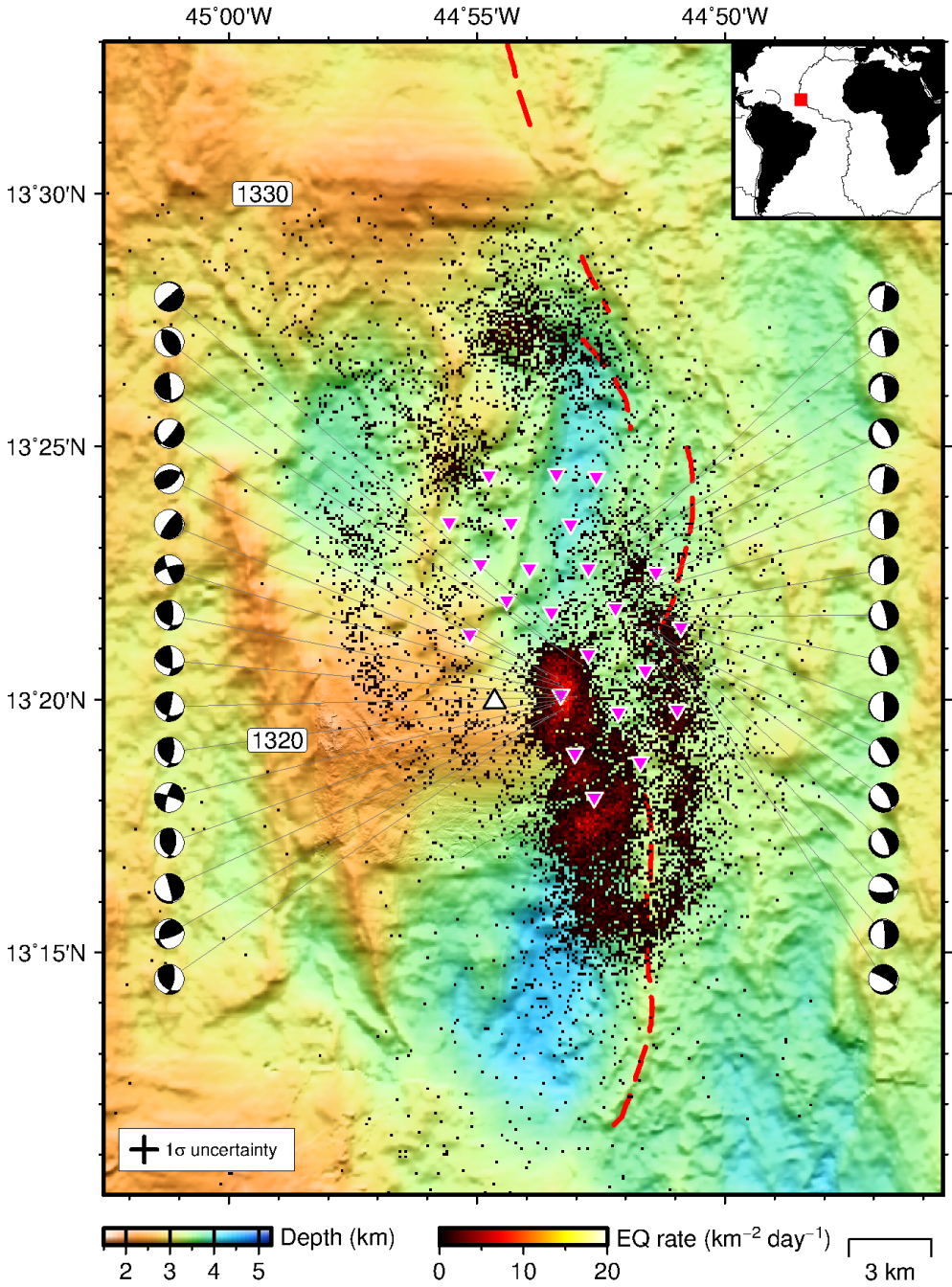

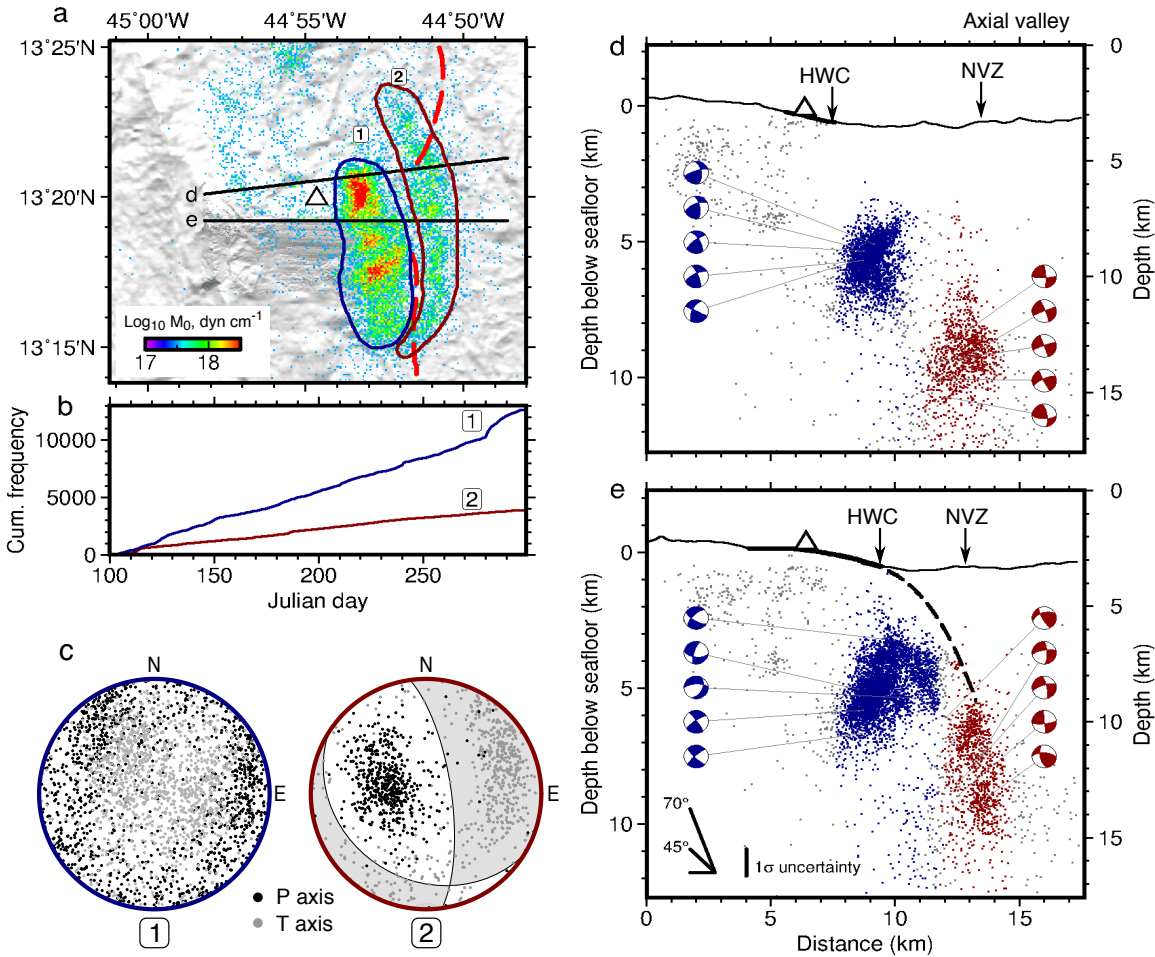

Figure 3

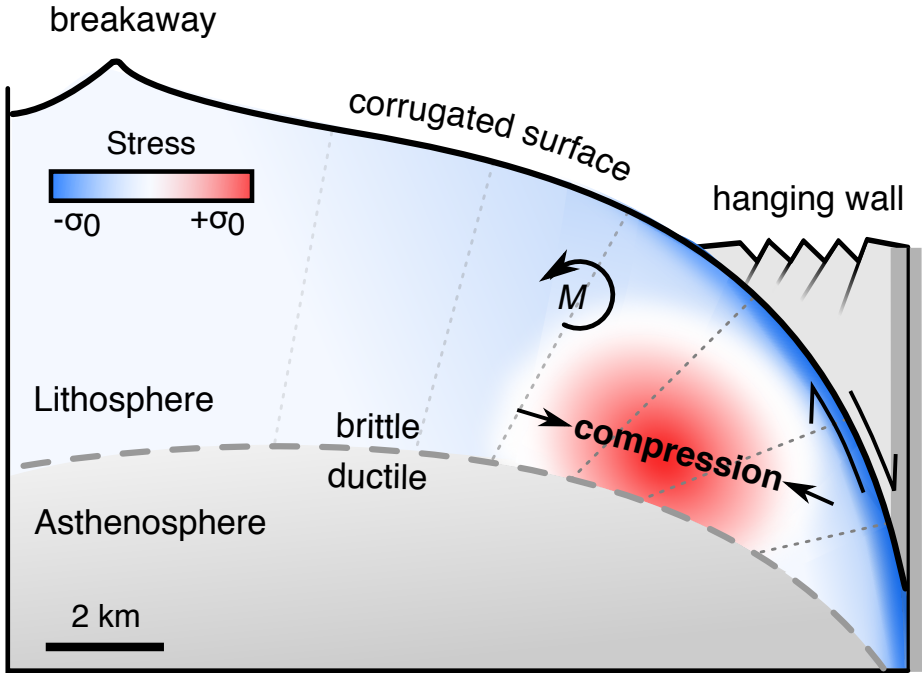

Oceanic Detachment Faults Generate Compression in Extension

R. Parnell-Turner[1], R. A. Sohn[1], C. Peirce[2], T. J. Reston[3], C. J. MacLeod[4], R. C. Searle[2] and N. M. Simão[2].

[1] *Department of Geology & Geophysics, Woods Hole Oceanographic Institution, Woods Hole Road, Woods Hole, MA 02543, USA*

[2] *Department of Earth Sciences, Durham University, South Road, Durham, DH1 3LE, UK*

[3] *School of Geography, Earth and Environmental Sciences, University of Birmingham, Birmingham B152TT, UK*

[3] *School of Earth, Ocean and Planetary Sciences, Cardiff University, Main Building, Park Place, Cardiff, CF10 3YE, UK*

SUPPLEMENTAL INFORMATION

DATA ACQUISITION AND PROCESSING

A network of 25, four-component, short period OBSs was deployed between April 12th and October 26th 2014. OBSs were free-fall deployed approximately 2-3 km apart, and 23 instruments successfully recorded data. Initial *P*- and *S*-wave arrivals were detected using an STA/LTA algorithm, and arrival times were refined with a kurtosis-based picking method (Supplementary Figs. 3 and 4; *Baillard et al.*, 2014). A one-dimensional *P*-wave velocity model was constructed using the median velocity obtained from a grid of coincident wide-angle seismic refraction profiles, and draped beneath the seabed (Supplementary Fig. 5; *Simão et al.*, 2016) This model was used to predict travel times between stations and nodes within a 70 x 70 x 20 km (*x*-*y*-*z*) model domain at 250 m intervals. An *S*-wave velocity model was generated with a V_p/V_s ratio of 1.8, obtained by minimizing root mean square (rms) arrival time residuals for V_p/V_s values ranging from 1.4 to 2.4. Travel times were calculated using an Eikonal finite-difference scheme and

NonLinLoc software (Podvin and Lecomte, 1991; Lomax et al., 2000). Initial earthquake locations were determined using the grid-search algorithm (Tarantola and Valette, 1982; Lomax et al., 2000) for 183,762 events detected by more than four OBSs. After applying stations corrections, double-difference hypocenter relocation was carried out for 35,262 well-constrained events detected on more than nine OBSs with rms residual < 0.15 s, using differential travel times from the catalog and the program hypoDD (Waldhauser and Ellsworth, 2000), yielding 18,313 double-difference relocated hypocenters. Best-fitting first-motion focal mechanism solutions for the subset of 35,262 relocated events were obtained using HASH software (Hardebeck and Shearer, 2002). The seismic moment for each event was calculated using the long-period spectral level of vertical displacement spectra, and then converted into a local magnitude estimate.

ELASTIC-PLASTIC MODEL

The model for elastic-plastic bending allows us to calculate synthetic profiles for the detachment footwall surface. The deflection of a bending plate is defined in terms of the bending moment, $M(x)$, which varies along the length of a bending profile, and the in-plane force, T, which is the horizontal force applied to the end of the plate, and is constant along a profile (Fig. 3). Far-field forces give rise to the in-plane force, which is applied from outside the bending region (e.g. ridge push). The rheological parameters are expressed in terms of the depths and horizontal normal stresses, $\sigma_{xx}(z)$ at the top and base of the elastic core (z_1 and z_2 respectively). Mathematical details of the model are described elsewhere (McAdoo et al., 1978). We require the deflected surface to dip at 20° at the point of emergence at the seabed, and to have a maximum slope of no greater than ~70° adjacent to the spreading axis. The problem is simplified by assuming a constant stress profile and a constant yield stress of 52 MPa. We assume a Young's modulus and Poisson's ratio of 60 GPa and 0.25, respectively, and a density contrast between lithosphere and water of 3800 kg m^{-3}. We vary the flexural rigidity of the bending plate, expressed in terms of T_e, in order to obtain a bending profile which best fits the observed seismicity and 20° dip of the corrugated surface on the seabed. T_e represents the

mechanical strength of a bending plate, which can be thought of as a response function that does not correlate to any geological or geophysical boundary within the lithosphere.

REFERENCES CITED

Baillard, C., Crawford, W.C., Ballu, V., Hibert, C., and Mangeney, A., 2014, An automatic kurtosis-based P-and S-phase picker designed for local seismic networks: Bull. Seismol. Soc. Am., v. 104, no. 1, p. 394–409, doi: 10.1785/0120120347.

Hardebeck, J.L., and Shearer, P.M., 2002, A new method for determining first-motion focal mechanisms: Bull. Seismol. Soc. Am., v. 92, no. 6, p. 2264–2276, doi: 10.1785/0120010200.

Lomax, A., Virieux, J., Volant, P., and Berge-Thierry, C., 2000, Probabilistic earthquake location in 3D and layered models, *in* Thurber, C.H. and Rabinowicz, N. eds., Advances in Seismic Event Location, Kluwer, Amsterdam, p. 101–134.

McAdoo, D.C., Caldwell, J.G., and Turcotte, D.L., 1978, On the elastic-perfectly plastic bending of the lithosphere under generalized loading with application to the Kuril Trench: Geophys. J. Int., v. 54, no. 1, p. 11–26, doi: 10.1111/j.1365-246X.1978.tb06753.x.

Podvin, P., and Lecomte, I., 1991, Finite difference computation of traveltimes in very contrasted velocity models: a massively parallel approach and its associated: Geophys. J. Int., v. 105, p. 271–284.

Simão, N., Peirce, C., Falder, M., Reston, T.J., Macleod, C.J., and Searle, R.C., 2016, Velocity structure of the crust at 13°N on the Mid-Atlantic Ridge: implications for crustal accretion and oceanic core complex formation: Abstract T33A-2997 presented at 2016 Fall Meeting, AGU, San Francisco, Calif. 12-16 Dec,.

Tarantola, A., and Valette, B., 1982, Generalized Nonlinear Inverse Problems Solved Using the Least Squares Criterion: Rev. Geophys., v. 20, no. 2, p. 219–232.

Waldhauser, F., and Ellsworth, W.L., 2000, A Double-Difference Earthquake Location Algorithm : Method and Application to the Northern Hayward Fault, California: Bull. Seismol. Soc. Am., v. 90, p. 1353–1368.

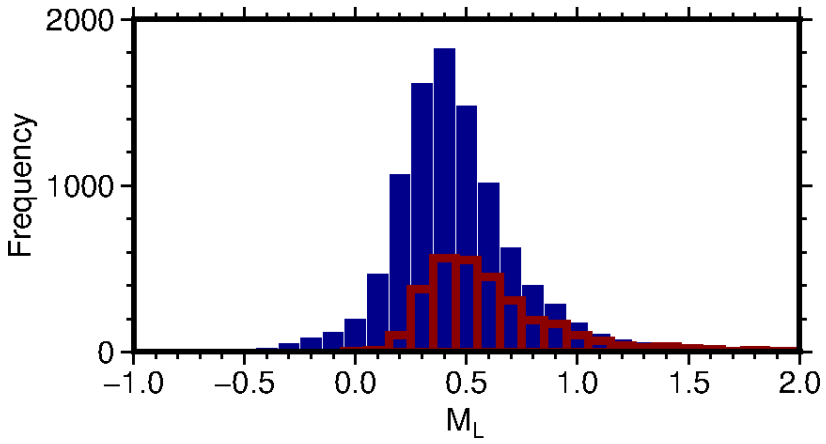

Supplementary Figure 1. Magnitude frequency histogram. Local magnitudes (M_L) calculated for relocated events detected by >9 stations. Blue bars are events from domain 1; red bars are from domain 2 (see Figure 2a for locations). M_L obtained from seismic moments, calculated using the long-period spectral level of vertical displacement spectra, and then converted into a local magnitude estimate. Cumulative moment release in domains 1 and 2 is 12.3 x 10^{20} and 7.7 x 10^{20} dyn cm^{-1}, respectively.

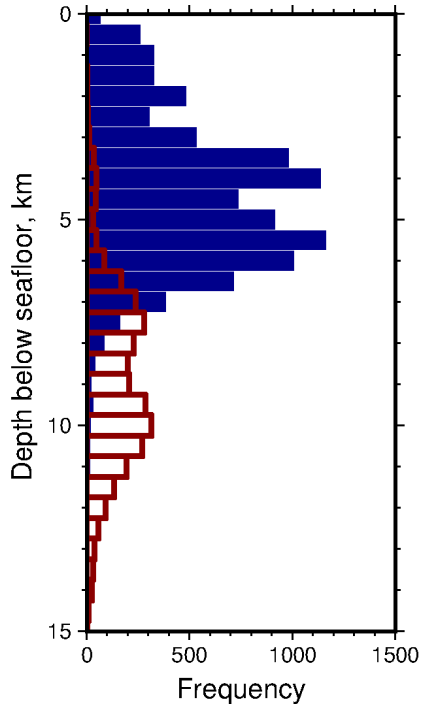

Supplementary Figure 2. Histogram of earthquake depths for domains 1 (blue) and 2 (red), see Figure 2a for locations.

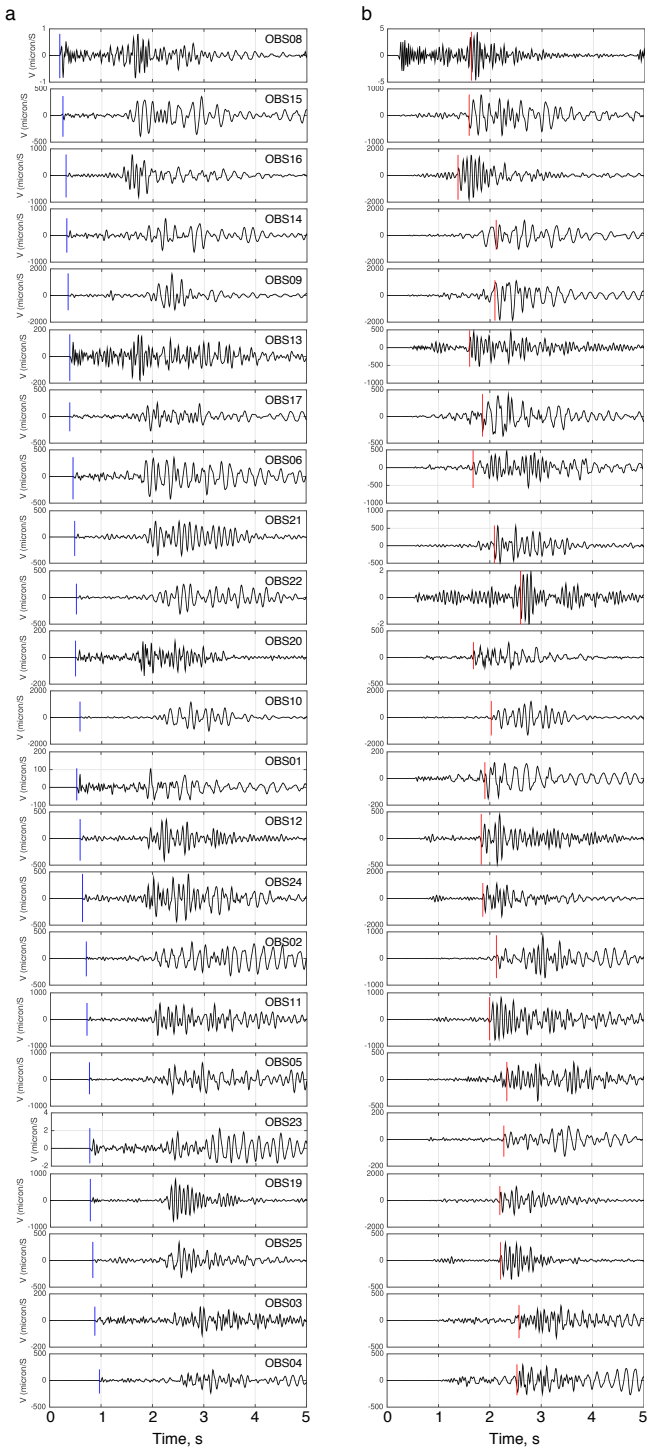

Supplementary Figure 3. Example seismograms and arrival picks for an extensional event located near the spreading axis. Event hypocenter at 13°21.298' N, 44° 52.030' W, depth below seabed 8.4 km, M_L = 1.7 at 05:48 UTC on 9th July 2014. a: Vertical component of velocity and compressional (*P*) wave phase picks (blue lines). b: Horizontal component of velocity and shear (*S*) wave phase picks (red lines). OBS numbers annotated, data band-pass filtered from 1-25 Hz.

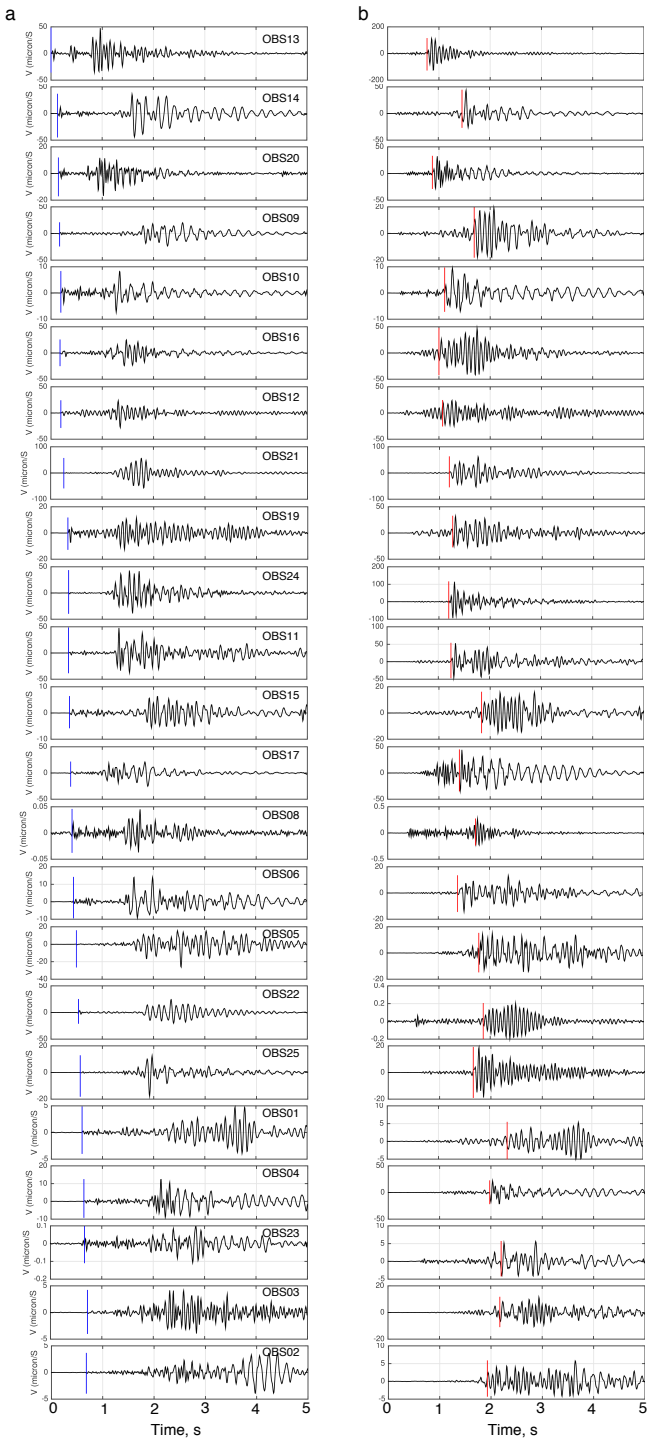

Supplementary Figure 4. Example seismograms and arrival picks for a compressional event located near the 13°20' N detachment fault. Event hypocenter at 13°20.740' N, 44°53.810' W, depth below seabed 4.8 km, M_L = 1.7 at 22:54 UTC on 29th June 2014. a: Vertical component of velocity and compressional (*P*) wave phase picks (blue lines). b: Horizontal component of velocity and shear (*S*) wave phase picks (red lines). OBS numbers annotated, data band-pass filtered from 1-25 Hz.

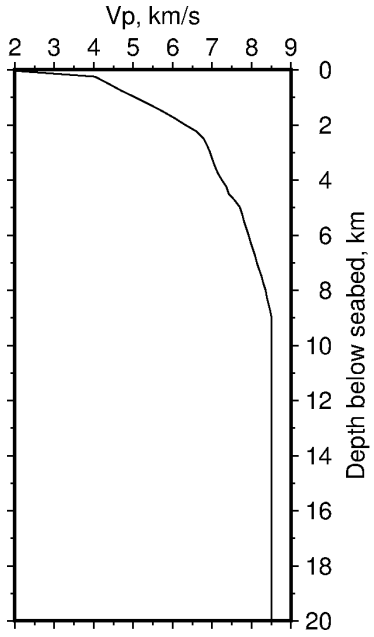

Supplementary Figure 5. *P*-wave velocity model used in the travel-time calculation. Model constructed by draping a median 1-dimensional *P*-wave model obtained from coincident wide-angle active-source seismic experiment (Simão et al., 2016).